AIP | Applied Physics Letters

Detection of electrically formed photosensitive area in Ca-doped BiFeO3 thin films

K. Kamala Bharathi, Won-Mo Lee, Ji Ho Sung, Ji Soo Lim, Seung Jin Kim et al.

Citation: Appl. Phys. Lett. **102**, 012908 (2013); doi: 10.1063/1.4774381
View online: http://dx.doi.org/10.1063/1.4774381
View Table of Contents: http://apl.aip.org/resource/1/APPLAB/v102/i1
Published by the American Institute of Physics.

Detection of electrically formed photosensitive area in Ca-doped $BiFeO_3$ thin films

K. Kamala Bharathi,[1] Won-Mo Lee,[2] Ji Ho Sung,[3] Ji Soo Lim,[1] Seung Jin Kim,[1] Kanghyun Chu,[1] Jung Won Park,[4] Jong Hyun Song,[4] Moon-Ho Jo,[3] and Chan-Ho Yang[1,5,a)]
[1]*Department of Physics, KAIST, Daejeon 305-701, South Korea*
[2]*Department of Materials Science and Engineering, Pohang University of Science and Technology (POSTECH), Pohang 790-784, South Korea*
[3]*Department of Materials Science and Engineering, Yonsei University, Seoul 120-749, South Korea*
[4]*Department of Physics, Chungnam National University, Daejeon 305-764, South Korea*
[5]*Institute for the NanoCentury, KAIST, Daejeon 305-701, South Korea*

(Received 13 November 2012; accepted 20 December 2012; published online 10 January 2013)

We report on the visualization of *n-p* junctions formed by oxygen vacancy movement under the application of an electric field in a Ca-doped $BiFeO_3$ thin film through spatially resolved scanning photocurrent mapping. The photocurrent mapping, in conjunction with the spectroscopic approach, provides clues to local electronic structures and defect levels associated with oxygen vacancies. These observations provide insights into the spatial redistribution of oxygen vacancies in an electric field. © *2013 American Institute of Physics*. [http://dx.doi.org/10.1063/1.4774381]

Recent advances in manipulating oxygen vacancies in transition metal oxides have contributed to the understanding of ionic effects, correlated electron effects, and their interplay.[1] Considerable attention has been paid to oxygen vacancy driven modifications of the magnetic, ferroelectric, and electronic properties of complex oxide materials.[2–7] Oxygen vacancies play critical roles in the resistive switching phenomena,[8] solid-oxide fuel cells,[9] electronic conduction at ferroelectric domain walls,[10] and in conducting oxide heterointerfaces.[11] Early fatigue issues in ferroelectric switching have also been attributed to oxygen vacancy aggregation near the metal electrode under *ac* electric fields.[2,12] Despite this attention, visualizations of the local electronic state associated with inhomogeneous oxygen vacancy distribution with spatial resolution are still lacking. This study uses a spatially resolved probing approach to examine the interplay of electronic state and oxygen vacancy density in a photo-induced current map. We focus on calcium-substituted bismuth ferrite, $Bi_{1-x}Ca_xFeO_{3-\delta}$ (BCFO), which is an oxygen vacancy ionic conductor. The parent $BiFeO_3$ (BFO) is a well-known multiferroic compound[13–16] that exhibits exotic photovoltaic and photocatalytic properties owing to its inversion symmetry breaking and narrow band gap.[17–20] Recently, it has been found that the substitution of calcium ions (Ca^{2+}) into Bi^{3+} positions causes the spontaneous formation of highly concentrated oxygen vacancies that compensate the Ca acceptors and maintain a stable Fe^{3+} valence state.[21–23] Another advantage of BCFO is that both *n*-type and *p*-type states are feasible by electrical control of local oxygen vacancy concentrations. It has been reported that the conductor–insulator transition occurs in the BCFO through band filling control.[22] Prominent electrochromism by means of vacancy order melting has also been observed in the compound.[23]

In this paper, we investigate the formation of *n-p* junctions and photo-induced charge separations in a BCFO thin film using the spatially resolved technique. This approach allows us to map the local photocurrent, wavelength-dependent photo-response, and its spatial variation across the *n-p* junction. We observe a large enhancement in the photocurrent at the depletion region and also detect the built-in electric field at the depletion region using electrostatic force microscopy (EFM). The observations are discussed on the basis of proposed electronic structure and optical transition. These investigations at a sub-micron scale of resolution provide clear signatures of the interplay between the oxygen vacancy migration and photo-induced conduction.

Epitaxial BCFO thin films (~160 nm in thickness) were grown on (001) $SrTiO_3$ (STO) substrates using pulsed laser deposition at 600 °C in 50 mTorr oxygen pressure using a KrF excimer laser (wavelength 248 nm). The laser repetition rate was 10 Hz and the laser energy was 140 mJ per pulse. Coplanar platinum electrodes were fabricated on the BCFO film. Electric forming between the co-planar electrodes was carried out by applying 30 V for 4 min at 200 °C. After the forming step, the sample was immediately quenched to room temperature to keep the formed state frozen in place. In the resulting BCFO film, spontaneously produced oxygen vacancies are randomly distributed over the film (Fig. 1(a)). With the application of electrical bias from the right to the left electrode, positively charged oxygen vacancies migrate in the electric field and accumulate near the negative electrode (Fig. 1(b)). This creates an *n*-type region at the donor rich area near the left electrode, and the opposite area becomes a *p*-type region. Fig. 1(c) shows an optical image of a formed area between the coplanar electrodes taken at room temperature. We can observe the peculiar feature of dark contrast only in the *p*-type region due to the increased concentration of free carriers, as reported in Ref. 23. Fig. 1(d) shows the *I-V* curve for a BCFO film measured at 200 °C. The shape of the *I-V* curve confirms the "switching diode"-like characteristics. As a result of the creation and inversion of the *n-p* junction, the polarity of the forward and backward bias can be reversed.

a)Author to whom correspondence should be addressed. Electronic mail: chyang@kaist.ac.kr.

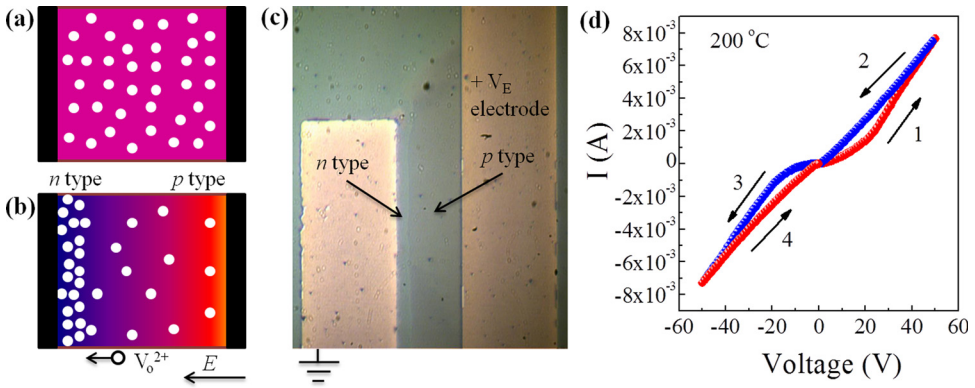

FIG. 1. (a) Schematic diagram describing the random distribution of oxygen vacancies in an as-grown BCFO thin film. (b) With the application of an electric field, positively charged donor oxygen vacancies move towards the negative electrode and create an *n*-type region. The opposite side becomes a *p*-type region. (c) An optical image of the region between the coplanar electrodes after 30 V has been applied for 4 min at 200 °C. (d) The *I-V* curve of a BCFO thin film measured at 200 °C. The sweeping sequence is indicated by the numbers and arrows.

To map the electrical field distribution over the formed BCFO film, we collected EFM measurements in ambient conditions. In the EFM measurements, the sample surface was scanned by a conducting tip with a positive voltage of 10 V at a height of 50 nm in non-contact mode. As shown in the schematic of the EFM measurement (Fig. 2(a)), electrostatic interaction between the electric field on the film surface and the tip voltage changes the resonant frequency of the tip vibration.[24] Using the lock-in technique to measure the change in the vibrating frequency of the tip, we were able to map the electric field distribution. Fig. 2(b) shows an EFM image of the area of a formed BCFO film close to the negatively biased electrode. The mapping clearly shows a different electrostatic force at the *n-p* junction. The depletion region is distinguished from *n*-type and *p*-type regions by a slightly higher frequency shift caused by tip vibration hardening. This confirms that the boundary between the *n*-type and *p*-type regions (depletion layer) lies close to the negatively biased electrode and the depletion region is spread over a few micrometers.

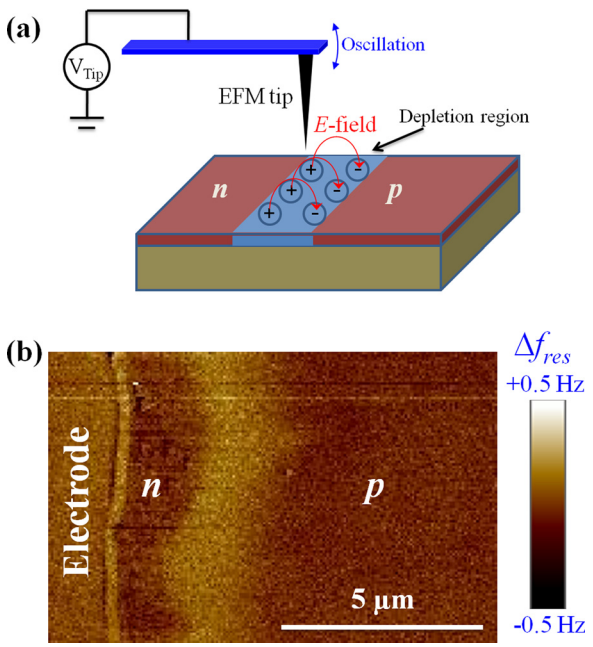

FIG. 2. (a) A schematic diagram of the EFM measurement. (b) An EFM image for a formed BCFO thin film covering the region near the negatively biased electrode. The depletion region is distinguished by contrasts in the frequency shifts of the resonant tip oscillation ($f_{res} \sim 102.73$ kHz) as a result of interaction with the built-in electric field.

Given the above results, we explored the photoresponses of the formed BCFO thin film. Spatially resolved scanning photocurrent maps were created using a focused light with a spatial resolution of ~500 nm. A BCFO sample was placed on a nm-scale controllable piezo-scanner, and with every change in its in-plane position, we measured the short-circuit photocurrent using the lock-in technique, as a function of the position of the focused laser spot, which was mechanically chopped at an excitation frequency of 100 Hz (Fig. 3(a)). Scanning photocurrent images of the area between the electrodes in the formed BCFO thin film are shown in Figs. 3(b) and 3(c). The color contrast indicates the spatial variation in the magnitude and direction of the short-circuit current. The magnitude of the short-circuit current varies gradually across the formed area and the highest value is recorded ~3 μm away from the negatively biased electrode. This corresponds to the area where the built-in electric field was detected in the above EFM measurement. Due to the built-in electric field that is created by carrier interdiffusion across the depletion region, photo-generated electron-hole pairs can be effectively separated and then transferred along the channel, which leads to the enhancement of the photocurrent.

To understand the electronic structure of the respective regions, we combined the spatially resolved technique with the spectroscopic approach. Wavelength-dependent short-circuit photocurrents were collected at different locations of light illumination across the formed electrodes, as shown in Fig. 4. The wavelength-dependent photocurrent at all measurement locations shows a large rise of approximately 2.67 eV, which corresponds to the optical transition from valence band to conduction band. The observed threshold energy is in good agreement with the optical gap reported for BFO at room temperature.[25,26] In addition to the large upturn caused by the inter-band transition, the abnormally large tail in the BCFO sample suggests that less pronounced shoulder peaks are present at ~2.43 eV. The occurrence of defect states and a sub-band feature is due to the presence of oxygen vacancies that have been previously reported in BFO.[26–28] In the present measurements, it is thought that oxygen vacancies produce the defect levels 0.2–0.4 eV below the conduction band minimum, and that the observed shoulder peaks are involved in the optical transition from the valence band to these defect levels. It is worth noting that the inter-band transition occurs at a relatively higher energy in the *p*-type regions than in the *n*-type regions, as indicated by the

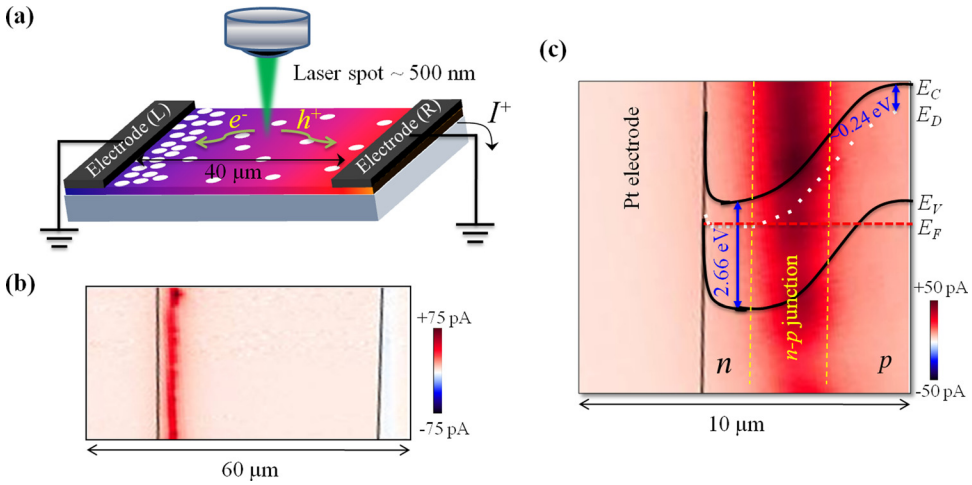

FIG. 3. (a) A schematic diagram describing the spatially resolved photocurrent experiment. (b) Spatially resolved scanning photocurrent image at room temperature for the formed BCFO thin film. Positive photo-induced short-circuit currents are denoted in red; photo-induced electrons move to the left electrode and holes move to the right due to the built-in potential at the boundary of the *n-p* junction. A laser wavelength of 460 nm with a power of 140 μW was used. (c) Photocurrent image along with the proposed band diagram across the film surface.

considerable shift in the absorption edge to the lower wavelength side.

To further explain the experimental observations, we discuss our intuitive understanding of the electronic structure of the BCFO compound. Similar to many late 3*d* transition metal oxides, BFO is a charge transfer-type insulator in which the conduction band is mainly composed of Fe 3*d* orbitals and the valence band is made of O 2*p* orbitals. As shown in Fig. 5, a single ionized oxygen vacancy strongly influences the 3*d* orbitals located at two neighboring Fe ions. As the oxygen vacancy produces effectively more positive potential, the level of the *d* orbitals near the defects becomes lower producing localized defect state while the others hybridize one another and form the conduction band. Therefore, introducing more oxygen vacancies increases the concentration of the localized mid-gap defect states. In the insulating state of $Bi_{1-x}Ca_xFeO_{3-\delta}$, which can be manifested by the balanced coexistence of Ca acceptor ions and oxygen vacancy donors ($\delta = x/2$), the Fermi level is between the defect states and the valence band maximum. In an oxygen vacancy rich regime ($\delta > x/2$), the Fermi level is laid on the defect levels. Although an ionized oxygen vacancy donates two electrons and pushes the band filling up, it also generates two more mid-gap states and thus the Fermi level can never be greater than the conduction band minimum. All of the *n*-type carriers are trapped in the localized *d* orbitals near oxygen vacancies, pinning the Fermi level to the associated defect levels. Additionally, the *p*-type doping, by decreasing the oxygen vacancy density ($\delta < x/2$), can freely decrease the Fermi level below the valence band maximum. Accordingly, the optical threshold in the *n*-type regions is a result of the optical *p-d* inter-site transition from valence band maximum to conduction band minimum and thus, it is expected to be nearly constant irrespective of the *n*-type carrier concentration. However, the threshold energies in the photocurrent measurement on the *p*-type doped regions can be attributed to the difference between the conduction band minimum and the Fermi level which is controllably lower than the valence band maximum. The threshold energy increases as the *p*-type carrier density increases. The

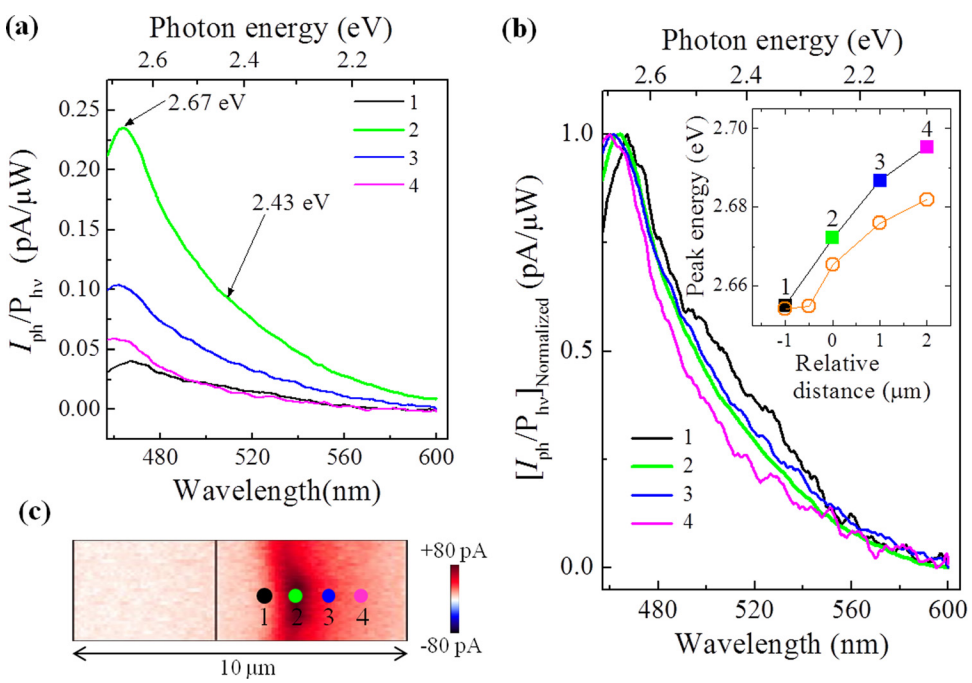

FIG. 4. (a) Wavelength-dependent photocurrents of a BCFO thin film from different locations around the depletion region. Shoulder peaks indicate the existence of mid-gap states due to oxygen vacancies. (b) Wavelength-dependent photocurrents normalized by each maximum value. The relative intensity of the shoulder peak increases systematically as the measurement position approaches the left electrode. In the inset, the photon energy giving the maximum photocurrent is plotted as a function of the relative light illumination position with respect to the *n-p* junction boundary. Similar independent measurements resulted in open circles. (c) Measurement positions are indicated.

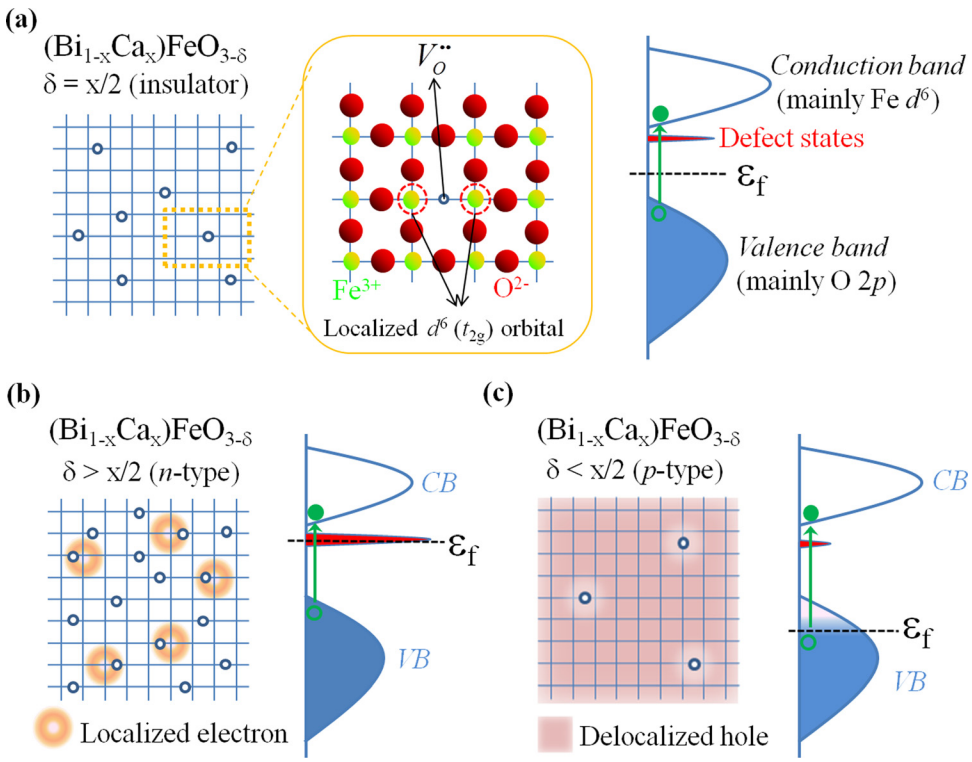

FIG. 5. (a) A schematic diagram of the FeO_2 plane of $Bi_{1-x}Ca_xFeO_{3-\delta}$ with oxygen vacancies and a density of electronic states in the insulating phase ($\delta = x/2$). An oxygen vacancy ($V_O^{\cdot\cdot}$) gives rise to the localization of d orbitals of neighboring Fe ions, producing defect states in the mid-gap. (b) In n-type doping cases ($\delta > x/2$), both the carrier concentration and the defect state density increase together with the oxygen vacancy density δ. The Fermi level lies at the defect levels partially occupying the defect states. (c) In p-type doping cases ($\delta < x/2$), the Fermi level is located below the valence band maximum and p-type carriers are delocalized.

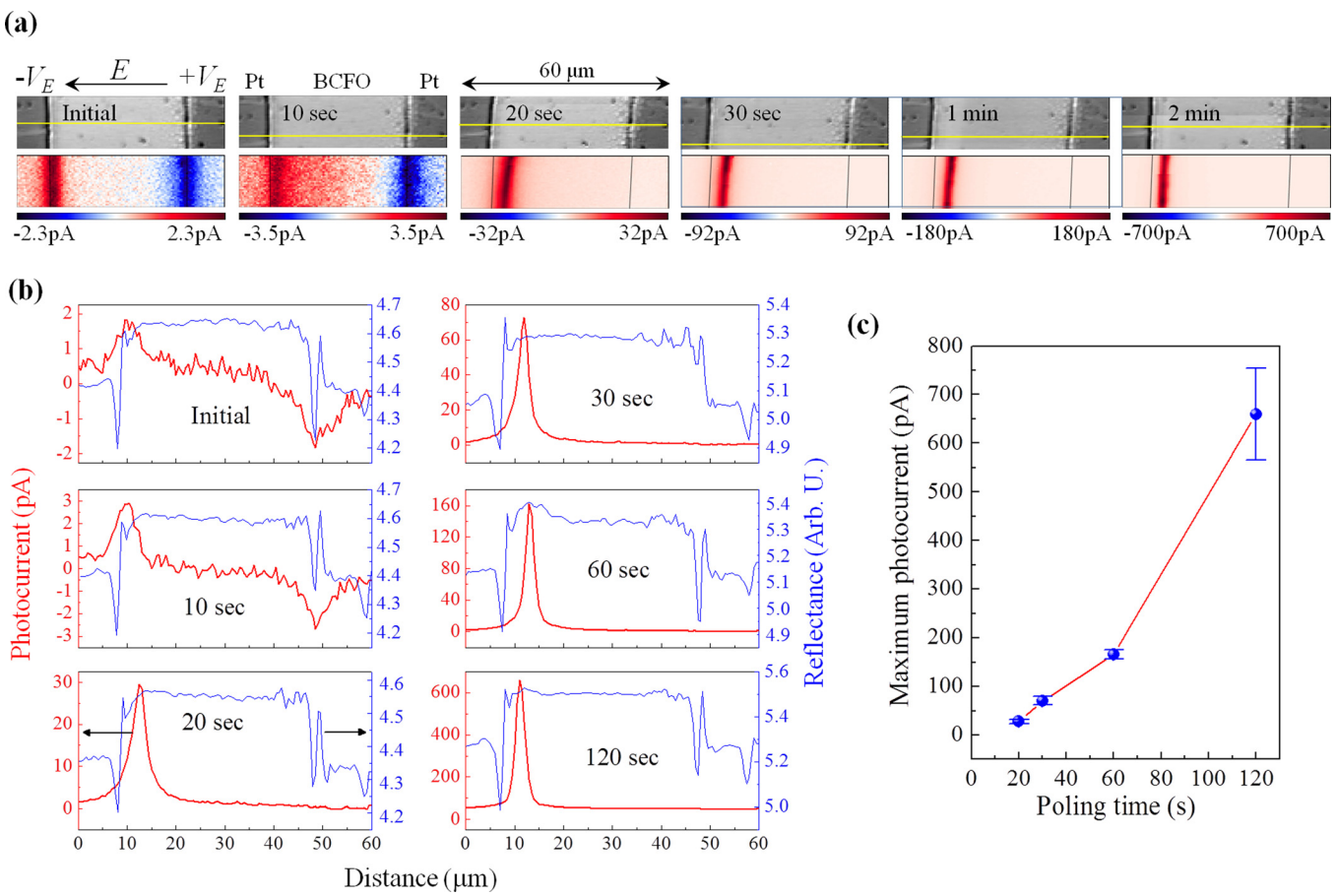

FIG. 6. (a) Reflectance and spatially resolved scanning photocurrent images of a BCFO film at room temperature measured subsequent to each 30 V forming, with various forming time intervals. We used a laser at a wavelength of 405 nm with a power of 1 mW. (b) Line profiles of the photocurrent across the formed area. The line along which the measurement was plotted is represented by yellow lines located along the same horizontal position in (a). (c) Maximum photocurrent (y) values are a function of forming time. Error bars (Δy) were calculated, using error propagation, to be $\Delta y = \frac{2|\Delta A|}{\pi w} + \frac{2A}{\pi w^2}|\Delta w|$, where ΔA and Δw represent the standard errors involved in the area and the peak width of the Lorentzian fit function.

proposed electronic structure and optical transition are consistent with the observed experimental shift of maximum photocurrent energy across the *n-p* junction.

In the final section, we discuss the effects of the forming time on electric formations conducted at an elevated temperature of 200 °C. Fig. 6(a) shows spatially resolved photocurrent images together with the reflectance images of BCFO samples with varying forming times. The reflectance images show the exact electrode edges and distinguish the sample surface by examining the distribution of impurities. Both the photocurrent and reflectance images were taken at as a reference before the forming process. Small photocurrents can be detected at both electrode edges. The magnitudes of the photocurrents are comparable, but the directions are opposite to each other. We note that the direction of the photocurrent at both electrodes is from the electrodes to the BCFO film. This is most likely because the as-grown state of BCFO films is slightly *p*-type doped. Considering that the electron affinity of BFO is known to be ~3.3 eV,[25] we can deduce that the work function of the *p*-type BCFO (~6 eV) is deeper than that of platinum (~5.6 eV). This results in a band bending, whereby photo-excited electrons flow into the nearby electrode and holes move in the opposite direction. The first forming process, at 10 s, did not result in a clear *n-p* junction formation. However, an *n-p* junction started to form in the 20-s forming process; a small but clear positive photocurrent (~28 pA) was observed, indicating the formation of a depletion region near the negatively biased electrode. The photosensitive region could be erased by annealing the film at 200 °C for one hour in an air environment as a result of thermalization of oxygen vacancy distribution. After using this technique to remove the *n-p* junction, a longer forming period was carried out and its photocurrent was mapped. The above sequence was repeated with forming times of 20, 30, 60, and 120 s. As the forming time increased (Fig. 6(a)), more oxygen vacancies piled up near the negative electrode, creating well-defined *n-p* junctions and narrowing the Shottkey barrier at both electrodes. Fig. 6(b) shows the line profile of the photocurrent across the formed area. Fig. 6(c) presents the maximum photocurrent as a function of the forming time. The photocurrent is largely enhanced from ~28 pA to ~660 pA, as the forming time increased from 20 to 120 s.

In summary, this study visualizes the *n-p* junction formation associated with oxygen vacancy migration. Using coplanar electrodes deposited on the surface of an as-grown BCFO film, we create *n-p* junctions with an electric forming process and then erase them with a thermal annealing process. The *I-V* measurements illustrate the diode-like features of the formed BCFO film, and EFM studies reveal the existence of a built-in potential at the depletion region. Using spatially resolved scanning photocurrent maps, we find that the depletion region near the negatively biased electrode is more photosensitive than the *n* and *p*-type regions. Wavelength-dependent photocurrent measurements reveal the formation of oxygen vacancy defect levels below the conduction band. Furthermore, the enhancement of the defect level at the *n*-type regions and the optical threshold energy shift to higher energy at the *p*-type regions are thought to be related to oxygen vacancy concentration and the peculiar inter-site *p-d* optical transition.

This work was supported by the National Research Foundation of Korea funded by the Ministry of Education, Science, and Technology (Contract Nos. 2010-0013528 and 2011-0016133). Work at KAIST was partially supported by the High Risk High Return Project. C.-H.Y. acknowledges support from the T. J. Park Science Fellowship. M.-H.J. acknowledges the support of the Basic Science Research Program (2010-0017853), Nano Original & Fundamental Technology R&D Program, Global Frontier Research Program (2011-0031639) through the NRF funded by the MEST.

[1]B. Keimer, J. Maier, and J. Mannhart, Nature Mater. **11**, 751 (2012).
[2]J. F. Scott and M. Dawber, Appl. Phys. Lett. **76**, 3801 (2000).
[3]C. Ederer and N. A. Spaldin, Phys. Rev. B **71**, 224103 (2005).
[4]X. Ren, Nature Mater. **3**, 91 (2004).
[5]R.-A. Eichel, J. Electroceram. **19**, 9 (2007).
[6]D. D. Cuong, B. Lee, K. M. Choi, H. S. Ahn, S. Han, and J. Lee, Phys. Rev. Lett. **98**, 115503 (2007).
[7]G. L. Yuan and A. Uedono, Appl. Phys. Lett. **94**, 132905 (2009).
[8]A. Sawa, Mater. Today **11**, 28 (2008).
[9]S. B. Adler, Chem. Rev. **104**, 4791 (2004).
[10]J. Seidel, P. Maksymovych, Y. Batra, A. Katan, S.-Y. Yang, Q. He, A. P. Baddorf, S. V. Kalinin, C.-H. Yang, J.-C. Yang *et al.*, Phys. Rev. Lett. **105**, 197603 (2010).
[11]W. Siemons, G. Koster, H. Yamamoto, W. A. Harrison, G. Lucovsky, T. H. Geballe, D. H. A. Blank, and M. R. Beasley, Phys. Rev. Lett. **98**, 196802 (2007).
[12]Q. Ke, X. Lou, Y. Wang, and J. Wang, Phys. Rev. B **82**, 024102 (2010).
[13]R. Ramesh and N. A. Spaldin, Nature Mater. **6**, 21 (2007).
[14]W. Eerenstein, N. D. Mathur, and J. F. Scott, Nature **442**, 759 (2006).
[15]R. J. Zeches, M. D. Rossell, J. X. Zhang, A. J. Hatt, Q. He, C.-H. Yang, A. Kumar, C. H. Wang, A. Melville, C. Adamo *et al.*, Science **326**, 977 (2009).
[16]K.-T. Ko, M. H. Jung, Q. He, J. H. Lee, C. S. Woo, K. Chu, J. Seidel, B. G. Jeon, Y. S. Oh, K. H. Kim *et al.*, Nat. Commun. **2**, 567 (2011).
[17]T. Choi, S. Lee, Y. J. Choi, V. Kiryukhin, and S.-W. Cheong, Science **324**, 63 (2009).
[18]S. Y. Yang, J. Seidel, S. J. Byrnes, P. Shafer, C.-H. Yang, M. D. Rossell, P. Yu, Y. H. Chu, J. F. Scott, J. W. Ager III *et al.*, Nat. Nanotechnol. **5**, 143 (2010).
[19]J. Seidel, D. Fu, S.-Y. Yang, E. Alarcón-Lladó, J. Wu, R. Ramesh, and J. W. Ager III, Phys. Rev. Lett. **107**, 126805 (2011).
[20]F. Gao, X. Chen, K. Yin, S. Dong, Z. Ren, F. Yuan, T. Yu, Z. Zou, and J.-M. Liu, Adv. Mater. **19**, 2889 (2007).
[21]D. Kothari, V. R. Reddy, A. Gupta, V. Sathe, A. Banerjee, S. M. Gupta, and A. M. Awasthi, Appl. Phys. Lett. **91**, 202505 (2007).
[22]C.-H. Yang, J. Seidel, S. Y. Kim, P. B. Rossen, P. Yu, M. Gajek, Y. H. Chu, L. W. Martin, M. B. Holcomb, Q. He *et al.*, Nature Mater. **8**, 485 (2009).
[23]J. Seidel, W. Luo, S. J. Suresha, P.-K. Nguyen, A. S. Lee, S.-Y. Kim, C.-H. Yang, S. J. Pennycook, S. T. Pantelides, J. F. Scott *et al.*, Nat. Commun. **3**, 799 (2012).
[24]J. Y. Son, G. Lee, and Y.-H. Shin, Appl. Phys. Lett. **94**, 162902 (2009).
[25]S. R. Basu, L. W. Martin, Y. H. Chu, M. Gajek, R. Ramesh, R. C. Rai, X. Xu, and J. L. Musfeldt, Appl. Phys. Lett. **92**, 091905 (2008).
[26]W. M. Lee, J. H. Sung, K. Chu, X. Moya, D. Lee, C. J. Kim, N. D. Mathur, S. W. Cheong, C.-H. Yang, and M. H. Jo, Adv. Mater. **24**, OP49 (2012).
[27]A. J. Hauser, J. Zhang, L. Mier, R. A. Ricciardo, P. M. Woodward, T. L. Gustafson, L. J. Brillson, and F. Y. Yang, Appl. Phys. Lett. **92**, 222901 (2008).
[28]S. J. Clark and J. Robertson, Appl. Phys. Lett. **94**, 022902 (2009).